# Differences in perchlorate adsorption to azobenzene monolayers on gold formed from thioacetate and thiol precursors

**MSc. Beibei Pang:** Max-Planck-Institut für Eisenforschung GmbH, Max-Planck-Str., 1, 40237 Düsseldorf, Germany

**Dr. Danish Iqbal:** Max-Planck-Institut für Eisenforschung GmbH, Max-Planck-Str., 1, 40237 Düsseldorf, Germany

**Dr. Adnan Sarfraz:** Max-Planck-Institut für Eisenforschung GmbH, Max-Planck-Str., 1, 40237 Düsseldorf, Germany

**Dr. P. Ulrich Biedermann:** Max-Planck-Institut für Eisenforschung GmbH, Max-Planck-Str., 1, 40237 Düsseldorf, Germany

**Prof. Dr. Andreas Erbe:** NTNU, Norwegian University of Science and Technology, Department of Materials Science and Engineering, 7491 Trondheim, Norway
E-Mail: azobenzene-sam@the-passivists.org

| | | |
|---|---|---|
| **MS-ID:** <br> Heft: / () | azobenzene-sam@the-passivists.org | May 13, 2022 |

**Abstract**

Modification of metal surfaces with complex molecules opens interesting opportunities to build additional functionality into these surfaces. In this work, self assembled monolayers (SAMs) based on the same photoswitchable azobenzene motif but with different head groups have been synthesized and their SAMs on Au(111)/Si substrates have been characterized. 3-[(4-phenylazo)phenoxyl]propyl thiol (PAPT) and its acetyl group protected analog, 3-[(4-phenylazo)phenoxyl]propyl thioacetate (PAPA), have been synthesized. SAMs from PAPT and PAPA have been characterized by infrared (IR) spectroscopy, X-ray photoelectron spectroscopy (XPS), ellipsometry and cyclic voltammetry (CV). The SAM-forming units of both SAMs are the same, as confirmed by IR and XPS, and the SAMs have similar surface coverage, as evidenced by analysis of the reductive desorption peaks in CVs. The tilt angle of the azobenzene moiety was ca. 75° with respect to the surface normal as determined by IR spectroscopy, i.e., the molecules are lying quite flat on the gold surface. Despite similar surface coverages, the CVs for PAPT in aqueous perchlorate solution show a typical perchlorate adsorption peak to gold, whereas the corresponding experiments with PAPA show no perchlorate adsorption at all. In conclusion, SAM formation can lead to an increase in the number of electrochemically accessible surface sites on the final, SAM covered surface. Whether the amount of such sites increases or decreases, depends on the precursor. The precursor most likely affects the adsorption mechanism and thus the atomic surface structure of the metal at the metal/SAM interface. Thus, details of the SAM formation mechanism, which is affected by the precursor used, can have quite strong effects on the electrochemical properties, and likely also electrocatalytic properties, of the resulting modified surface.

# 1   Introduction

Self-assembled monolayers (SAMs) have been intensively investigated for surface modification, among others, in nanotechnology [1–4], biotechnology [4–8], electronics [9, 10], and corrosion protection [11–14]. A typical preparation for SAMs is the direct immersion of a substrate into a thiol solution for a certain amount of time. However, thiols tend to oxidize in the presence of oxygen [15]. One alternative to prepare SAMs is to substitute the hydrogen atom with a cleavable protective group on the thiol's sulfur atom [16–18]. As one specific example, the acetyl group in thioacetates can be cleaved in certain solvents [19].

In earlier investigations, SAMs prepared from thiol and its corresponding thioacetate were considered to possess the same structures [20]. Later investigations reported highly ordered SAMs prepared from thioacetates [16, 18, 21, 22]. More recent work showed that SAMs prepared from thiol and its corresponding thioacetate have different structures; SAMs prepared from thioacetate showed significantly larger domains, a different crystallographic structure and overall a higher order [21]. Thioacetates are interesting precursors for SAMs because of the increased stability towards oxidation compared to thiols, while at the same time the basic surface properties are expected to be conserved [16].

Complex SAM forming units enable an interesting class of responsive surfaces [23, 24], though such surface modification does not always yield the intended molecular structures at the interface [25]. A prototypical example for SAMs with complex molecular building blocks is based on a photoisomerisable aromatic motif, interesting, e.g., for applications in molecular electronics [10]. The conformation change of photosensitive molecules, often azobenzene-based, in SAMs is typically constrained by steric requirements [26, 27], but collective effects in the excitation also play a role [27–29]. Spacious anchoring groups — not necessarily thiolate-based — ensure reversible photoswitching [30, 31]. Likewise, appropriate solvent selection can be used to ensure photoisomerisation [27]. Conformational switching barriers depend on the environment [32]. Azobenzenes also have interesting non-linear optical properties [33, 34]. Issues with thermal conformation switching may be avoided by using stilbene or hydrazone moieties [35–38]. With their aromatic moieties and their corresponding electronic structure, electrochemical properties of SAMs with isomerisable aromatic moieties are also interesting to investigate.

The presence of SAMs on metal electrode surfaces normally leads to blocking of metal oxidation or metal dissolution [11, 39, 40], however, also the increase of reactivity, e.g. towards hydrogen evolution, has been observed [41, 42]. In alkyl of hydroxyalkyl SAMs, the beginning hydrogen evolution can stabilize "hemi-micelle-like"-structures at the surface after electrochemical desorption [43]. Anion adsorption was found to be suppressed by a saccharide based SAMs [44]. The investigation of electrochemical properties of SAM modified electrodes is thus often leading

to unexpected results.

In this work, the effect of the end-group on the surface structure of azobenzene-containing SAMs was studied, including the electrochemical properties. To that end, 3-[(4-phenylazo)phenoxyl]propyl thiol (PAPT) and its acetyl protected analog, 3-[(4-phenylazo)phenoxyl]propyl thioacetate (PAPA), have been synthesized and used to prepare SAMs on evaporated gold, typically dominated by Au(111) surfaces, on silicon substrates. Both SAMs were characterized with ellipsometry, X-ray photoelectron spectroscopy (XPS), and infrared (IR) spectroscopy. By measuring cyclic voltammograms (CVs), the reductive desorption of both SAMs, and ion adsorption from the electrolyte of both SAMs have been investigated and compared.

# 2 Materials and methods

The synthesis procedure used in this work (Fig. 1 and Fig. 2) is a modification of a procedure from the literature [45]. All commercial ingredients were used as received.

## 2.1 Synthesis of [4-(phenylazo)phenoxy]propane-1-thiol

### 2.1.1 Synthesis of 4-(3-bromopropanoxy)-diazobenzene (1)

3.96 g (0.02 mol) 4-phenylazophenol, 6.1 mL (0.06 mol) 1,3-dibromopropane and 5.53 g (0.04 mol) $K_2CO_3$ were refluxed in 60 mL acetone at 80 °C for 6 h. Subsequently, 125 mL deionized water were added. The resulting precipitate was collected, and purified by silica column chromatography, using heptane and chloroform (volume ratio 2:1) as eluent. The first fraction ($R_f = 0.67$) was collected, the solvent evaporated and the remainder dried at 70 °C under vacuum. The orange colored crystals (**1**; Fig. 1) (2.5 g, 40% yield) were used for subsequent synthesis.

$^1$H-NMR (CDCl$_3$): $\delta = 2.27$ ppm (m, 2H, aliphatic CH$_2$), 3.54 ppm (t, 2H, BrC**H**$_2$), 4.11 ppm (t, 2H, OC**H**$_2$), 6.93 ppm (m, 2H, aromatic), 7.40 ppm (m, 3H, aromatic), 7.81 ppm (m, 4H, aromatic).

### 2.1.2 Synthesis of [4-(phenylazo)phenoxy]propane-1-isothiouronium bromide (2)

This reaction was carried out under argon atmosphere. 2.50 g (7.83 mmol) 4-(3-bromopropanoxy)-diazobenzene (**1**; Fig. 1) and 0.76 g (10.00 mmol) thiourea were refluxed in 80 mL degassed absolute ethanol at 85 °C for 6 h. After evaporation of the solvent, the residue was recrystallized from heptane/ethanol (volume ratio 1:1). The precipitate was collected by vacuum filtration and dried at 60 °C under vacuum. The product (**2**; Fig. 1) (2.0 g, 66% yield) was orange colored and was used in the next step.

4

$^1$H-NMR (DMSO-d$_6$): $\delta$ = 2.17 ppm (m, 2H, aliphatic C**H**$_2$), 3.40 ppm (t, 2H, SC**H**$_2$), 4.25 ppm (t, 2H, OC**H**$_2$), 7.22 ppm (m, 2H, aromatic), 7.62 ppm (m, 3H, aromatic), 7.93 ppm (m, 4H, aromatic), 9.14 ppm (s, 4H, N**H**$_2$).

### 2.1.3 Synthesis of [4-(phenylazo)phenoxy]propane-1-thiol (3)

2.05 g (5.19 mmol) [4-(phenylazo)phenoxy]propane-1-isothiouronium bromide (**2**; Fig. 1) was refluxed in 100 mL absolute ethanol with aqueous sodium hydroxide (0.62 g, 15.50 mmol) at 85 °C for 3 h. Diluted sulfuric acid was added until pH 3. The mixture was then extracted with diethyl ether. The organic phase was collected and dried over anhydrous sodium sulfate. Subsequently, the ether was evaporated, the residue was purified by silica column chromatography with heptane/dichloromethane (volume ratio 1:2) as eluent. The first fraction ($R_f$ = 0.41) was collected and dried at 75 °C under vacuum. The product (**3**; Fig. 1) (0.72 g, 51% yield) was an orange colored powder.

$^1$H-NMR (CDCl$_3$): $\delta$ = 1.31 ppm (t, 1H, S**H**), 2.06 ppm (m, 2H, aliphatic C**H**$_2$), 2.70 ppm (t, 2H, SC**H**$_2$), 4.10 ppm (t, 2H, OC**H**$_2$), 6.94 ppm (m, 2H, aromatic), 7.40 ppm (m, 3H, aromatic), 7.82 ppm (m, 4H, aromatic).

## 2.2 Synthesis of 3-[4-(phenylazo)phenoxy] propyl thioacetate (4)

6.64 g (48.02 mmol) K$_2$CO$_3$ and 2.34 g (11.80 mmol) 4-phenyl-azophenol were dissolved in 200 mL dimethylformamide. 5 mL (37.97 mmol) 3-chloropropyl thioacetate were added into the mixture while stirring. The mixture was refluxed at 100 °C overnight under exclusion of light. The reaction mixture was separated by silica column chromatography using heptane/ethyl acetate (volume ratio 7:3) as eluent. The first fraction ($R_f$ = 0.55) was collected and dried at 75 °C under vacuum. The final product (**4**; Fig. 2) was a sticky orange powder and was stored for further use.

$^1$H-NMR (CDCl$_3$): $\delta$ = 2.03 ppm (m, 2H, aliphatic C**H**$_2$), 2.26 ppm (s, 3H, -C**H**$_3$), 3.02 ppm (t, 2H, -C**H**$_2$-S-), 4.03 ppm (t, 2H, -O-C**H**$_2$), 6.93 ppm (m, 2H, aromatic), 7.42 ppm (m, 3H, aromatic), 7.83 ppm (m, 4H, aromatic)

## 2.3 Substrate preparation

Au(111)/Si substrates were prepared by evaporating 5 nm chromium and 100 nm gold onto clean silicon wafers at a base pressure below $10^{-6}$ mbar. SAMs were prepared by immersing Au(111)/Si substrates in 10 $\mu$M ethanolic solution of PAPT or PAPA overnight. Subsequently, Au(111)/Si substrates were rinsed with ethanol for 5 min and dried with a nitrogen

stream. 20 $\mu$L of a 10 mM solution of triethylamine were added to the
PAPA solution as cleavage agent.

## 2.4 Surface characterization

### 2.4.1 IR spectroscopy

IR spectra were recorded under vacuum with a Bruker Vertex 70v spectrometer equipped with a liquid nitrogen cooled MCT detector. KBr
pellets were measured in transmission mode. SAMs were measured in reflection with a p-polarized beam at an incidence angle of 80° with respect
to the surface normal. Background for SAMs measurements were bare
Au(111)/Si substrates cleaned with ethanol. All spectra were measured
with a resolution of 4 cm$^{-1}$.

In the SAMs, the average tilt angle $\delta$ of the long axis in SAMs forming
molecules indicated in Fig. 1 and Fig. 2 with respect to the Au(111) surface
normal was calculated based on IR spectra using [46]

$$\langle \cos^2 \delta \rangle_N = \frac{D^{(\mathrm{refl})}}{D^{(\mathrm{refl})} + 2D^{(\mathrm{trans})}}. \tag{1}$$

In this calculation, the absorbance ratio $D = A_{\parallel}/A_{\perp}$ of absorbance $A_{\parallel}$
of a mode with transition dipole moment (TDM) parallel to the long axis
of the molecule and absorbance $A_{\perp}$ of a mode with TDM perpendicular
to the long axis was used. The orientation of the TDM was taken from
DFT calculations of the model compound shown in Fig. 5.

Several different methods to determine absorbance for quantitative
analysis have been evaluated, e.g. using peak absorbance over baseline,
and integrated absorbance after different methods of baseline correction.
The tilt angles obtained via the different methods agreed to within 5°; here
the results from the simplest method, using peak absorbance, are reported.
$D^{(\mathrm{refl})}$ was obtained from SAM spectra, while $D^{(\mathrm{trans})}$ was obtained from
the respective absorption modes in KBr pellet spectra. By using tilt
angles determined this way and a molecular length $l = 1.5$ nm from the
molecular model, the thickness $t^{(\mathrm{IR})}$ of the two SAMs were estimated as

$$t^{(\mathrm{IR})} = l \cos \delta. \tag{2}$$

### 2.4.2 Ellipsometry

A Sentech SE800 spectroscopic ellipsometer with a Xenon light source was
used to determine monolayer thickness $t^{(\mathrm{ell})}$. Ellipsometric parameters
were acquired from 550 to 800 nm at an incidence angle of 70° with
respect to the surface normal. In this spectral range, thiol and thioacetate
are considered to be transparent, so the imaginary part of the refractive
index was neglected in the data fitting process. The real refractive index
was assumed to be 1.45 [45]. The data were modeled with a three phase

(ambient-SAM-substrate) model. The thickness was obtained as average result of 10 measurements. Uncertainty is presented as single standard deviation.

### 2.4.3 XPS

XPS was measured with a Physical Electronics Quantum 2000 spectrometer. A monochromatic Al $K_\alpha$ source was used for excitation. The incidence angle was 45°. The binding energy scale was referenced to the Au $4f_{7/2}$ substrate level at 84.0 eV [47, 48]. Spectra were analyzed using CasaXPS (http://www.casaxps.com/).

### 2.4.4 CV

CV experiments were carried out with a three-electrode cell connected to an Ivium CompactStat potentiostat. The electrolyte was purged with nitrogen gas for 1 h before measurements. Pt was used as counter electrode, together with an Ag/AgCl/3M KCl commercial reference electrode (Metrohm). All electrode potentials in this work are reported with respect to Ag/AgCl/3M KCl. Electrode area was 0.78 cm$^2$.

## 2.5 DFT calculations

For assignment of the IR spectra, 4-methoxy-diazobenzene was used as model for the azobenzene core (see section 3.1). The molecule was fully optimized using the hybrid density functional B3-LYP and the cc-pVTZ basis set as implemented in Turbomole version 6.2 (http://www.turbomole.com) [49]. The calculated harmonic vibrational frequencies were scaled by 0.9691 to correct for systematic errors in DFT and anharmonicity [50].

# 3 Results and discussion

## 3.1 SAM characterization

Fig. 3 shows XP spectra of the S 2p energy region in PAPT and PAPA SAMs. The S 2p signals in both SAMs consist of a single peak with asymmetry because of the $2p_{1/2}$ and $2p_{3/2}$ components. The maximum of these components is at $\approx$163 eV and 162 eV, respectively. Consequently, the sulfur is predominantly bound to the surface (see, e.g., comparison and discussion in [35]). The XPS analysis did, however, not yield a clear picture of the surface composition, in part due to the high noise level in spectral regions characteristic for S, N and partly O. The expected atomic ratio C:N:O:S is 15:2:1:1 in the SAM, and for PAPT, values of 20...40:1.9-4.8:1.2-2.9:1 were found when normalising to sulfur. For PAPA, the resulting ratio was 6.5:0.3:1.4:1. Carbon is thus always the most prominent element, as expected. However, the carbon content in PAPT is higher

7

than expected, which may be caused by adsorption of "adventicious" carbon, in addition to the shielding of deeper lying parts of the SAM by carbon. Also the oxygen content is consistently higher than expected, which may also be related to impurity adsorption. In PAPT, the N:S ratio includes the expected interval. In PAPA on the other hand, more sulfur was present on the surface than expected.

SAM IR spectra and corresponding bulk spectra are displayed in Fig. 4. The assignments of selected, important and characteristic IR peaks and peak wavenumber as obtained from DFT calculations are given in Tab. 1.

## 3.2 Electrochemical properties

In Fig. 6, cathodic desorption peaks at -1.07 V originate from the reductive desorption, $Au-S-R + e^- \longrightarrow Au + RS^-$ [40, 41, 43]. Since the surface structure has been modified after the first scan, only the first scan is used for surface coverage calculation via an integration of the peak current over time. Charges obtained by integration of the desorption peaks are listed in Tab. 2.

Fig. 7 shows CVs in a potential range where typically adsorption and desorption of perchlorate is observed on Au(111) [51, 52]. The peak is weakly visible on unmodified Au(111), it is enhanced in the presence of PAPT SAMs, and it is almost completely suppressed on PAPA-covered electrodes. Thus, the interaction between $ClO_4^-$ ions and the surface is enhanced on PAPT SAM modified surfaces while the adsorption of $ClO_4^-$ ion is suppressed in the case of PAPA SAMs. Charges obtained by integration of the CV peaks are listed in Tab. 2.

## 3.3 SAM structure

Compared with IR spectra in KBr pellets, only specific vibrations show absorptions in SAM spectra, leading to modified peak absorbances as shown in Fig. 4. The most striking difference in the PAPA spectra is the absence in the SAM spectra of the peak at 1697 cm$^{-1}$ which is one of the strongest in the KBr spectrum; this peak is in a region typical for the C=O stretching modes of carboxyl groups, and is thus assigned to the thioacetate's carboxyl C=O stretch. Further differences between IR spectra in KBr pellets and SAMs are caused by the alignment of the molecules on the Au(111) surface and the "surface selection rule" (e.g., [46] for an introduction). The characteristic aromatic ring modes at ≈1600, ≈1580 and ≈1500 cm$^{-1}$ are still detected in the SAMs, but are much less prominent compared to the dominating C-O-C$_{ar}$ mode. On the other hand, the aromatic bending modes e and f are more prominent in the SAM spectra. Since the aromatic ring stretching modes have TDMs oriented approximately along the molecular $C_1$-$C_4$ axis (Fig. 1 and 2), while the bending modes have TDMs approximately perpendicular to this axis, the

8

molecules must have a high tilt angle toward the surface normal. This angle will be quantified below.

In both SAM spectra and KBr spectra, the strongest peak must be related to the bond stretching involving the C-O bonds. In contrast to the aromatic ring modes, this mode is shifted by ca. $15$ cm$^{-1}$ when comparing SAM and KBr bulk spectra. Such a shift indicates already a difference in conformation when comparing bulk and SAM, and a conformational difference becomes more obvious when comparing the absorbance ratios in the SAMs and in the KBr spectra. In the conformation shown in Fig. 5, the TDMs of modes designated as a, b, c and d are in good approximation parallel to each other. If the TDMs are parallel, the peak absorbance should have the same ratio in both KBr and SAM. However, when analyzing the IR spectra in more detail, significant differences of peak absorbance are visible when comparing the different peaks. These differences in relative absorbance are particularly obvious when comparing modes a, b and c with modes e and f. While a, b and c still have approximately the same absorbance ratio in the SAM, mode d stands out. Since mode d is predominantly the $C_4$-O-C stretching mode, we can conclude that around the $C_4$-O bond, a different conformation must dominate both PAPT and PAPA SAMs, compared to the situation in the solid which is probed by the KBr spectra.

Using eq. (1), tilt angles for the different combinations of TDMs have been obtained (Tab. 3), showing that the aromatic moieties are tilted ca. $75°$, while the $C_4$-O-C TDM is tilted at ca. $60°$, indicating a "bending" of the molecule. There is a rather large non-symmetric uncertainty when expressing the results in angles, because of the $\cos^2$ dependence in eq. (1). Therefore, these numbers are given only approximately (see caption of Tab. 3).

Even though the SAM-forming unit is the same for both PAPT and PAPA, it is clear that PAPT SAMs and PAPA SAMs have different surface structures. Quantitative parameters are compiled in Tab. 3. PAPT SAMs are apparently thicker than PAPA SAMs. Nevertheless, there is little difference between the tilt angles of the aromatic moieties between of the two structures. For PAPA SAMs, the calculated tilt angles and thicknesses from IR and ellipsometry agree with each other, which isn't the case for PAPT. Differences may be caused by neglecting the optical anisotropy (birefringence) of the films in the ellipsometry analysis. Especially for small thicknesses, such effects may become considerable (see, e.g., formalism developed in [43]). Importantly, the "internally referenced" determination of tilt angles of important molecular quantities by IR shows no major differences between the systems, so that effects of birefringence appear unlikely as explanation of the observed differences in ellipsometric experiments. The differences in PAPT may also indicate that the simplified packing model which is the basis for relating thickness and tilt does not hold. For similar SAM systems, the work function which would affect electrochemical behavior has been systematically in-

9

vestigated with variation in the composition; based on the magnitude of effects observed there, we do not expect significant changes between the two SAMs investigated here [53].

Surface coverage for each SAM (Tab. 3) was calculated from electrochemical desorption results; the ellipsometric thickness is also related to surface coverage. It is worth noting that SAMs may not be completely desorbed during the first CV scan [39]. Uncertainties of the CV-determined surface coverages are rather high; within these high uncertainties, the SAM surface coverages show no significant difference. These high uncertainties originate from comparatively large differences between different repeats, indicating different amounts of of surface defects in the different repeat preparations. Larger differences between PAPA- and PAPT-derived SAMs and lower uncertainty was observed in the ellipsometric experiments. Ellipsometric experiments may be interpreted such that molecules in PAPA SAMs are less densely packed, when assuming an isotropic SAM. While the CV surface coverages show rather large uncertainties, the uncertainties in the ellipsometric measurements is so low that the differences between the SAMs can be regarded as statistically significant, assuming similar effects of the systematic errors (see previous paragraph). Even if there was a difference in the systematic errors, the statistically significant difference between the two types of SAMs investigated here would indicate differences in SAM-structure. While the observed differences may also be related to birefringence (see discussion in [43]), such an effect should lead to differences in the IR-determined tilt angles between PAPT and PAPA. The lower packing density in PAPA, however, does not manifest itself in higher tilt angles as determined via IR. As a consequence, there must be other differences in the packing, leaving more space at the surface and more accessible gold atoms. The larger available space leads to the different electrochemical properties of the observed SAMs.

In the CVs in Fig. 7, a pair of peaks at 0.35 V and 0.18 V are assigned to the adsorption and desorption of $ClO_4^-$ ions, respectively [51, 52]. A comparison of these peaks show that despite only minor differences in surface coverage PAPA SAMs suppress the interaction between $ClO_4^-$ ion and Au(111) surface, whereas PAPT SAMs facilitate adsorption, which is counterintuitive. The charges of $ClO_4^-$ ad- and desorption (Tab. 2) are one order of magnitude lower than the charges associated with the reductive desorption of the SAMs. Such an order of magnitude is reasonable, as the available surface area for perchlorate adsorption should remain lower than the area used by the SAMs. A schematic representation of the results is shown in Fig. 8. Different possible reasons shall be discussed in the following to explain the different perchlorate adsorption.

There is no direct evidence from IR or XPS for the presence of further components in the PAPA SAMs, though such an impurity cannot be ruled out. Immediate candidates would be the acetate ion and triethylamine, the base used for cleavage. The presence of acetate should (if not in very

10

unusual orientation) show up by a quite strong and well-defined carbonyl peak in the IR, which in the IR of PAPA SAMs (Fig. 4) is neither observed in the range around 1710 cm$^{-1}$ (carboxylic acid, -COOH) nor around 1590 cm$^{-1}$ (antisymmetric COO stretch of the carboxylate ion, $-COO^-$). Residual ethanol solvent cannot be completely excluded, but the solvent is not known to chemisorb to gold. In the case of triethylamine adsorption, a larger nitrogen content in the XPS would be expected, but the XPS results rather showed a much stronger sulfur signal than expected. The only type of impurity possible from these results is thus a sulfur-rich impurity, which must be sulfidic in nature (c.f. XPS S 2p), and not give significant peaks in the IR; a possible candidate would be adsorbed sulfide. Adsorbed sulfide should also show in the electrochemical reductive desorption experiments, where no additional peak was found, and the amount of charge that could be in the desorption of such an impurity can be in first approximation estimated to be the difference between the desorption current of PAPT and PAPA. This difference is on the order of 20%, and its magnitude is also similar to the perchlorate ad- and desorption charges in PAPA. This amount of impurity is too low to explain the deviations in the S:N ratio in XPS for PAPA. Thus, if this sulfide-rich impurity would not specifically block adsorption sites of perchlorate, its presence is unlikely to explain the observed effect.

Furthermore, it is not likely that perchlorate binds to other parts of the PAPA/PAPT molecules, and even if, no differences of the ion adsorption behavior would result from such a binding unless structural differences between the SAMs facilitate such binding.

Alternatively, the domain structure of the two SAMs may be different, and $ClO_4^-$ may adsorb only at domain boundaries, which then must be more abundant, or more accessible, in PAPT. However, such an explanation cannot account for the larger peak current when comparing PAPT to Au(111). Instead, in such a mechanism, an adsorption charge lower than that on Au(111) would be expected.

In that context, it is worth noting that the comparison to the adsorption and desorption current on unmodified Au(111) may be misleading, as these surfaces have been handled through ambient atmosphere, and have been solvent treated. Therefore, they are likely covered with some loosely bound organic adsorbate which could in principle affect adsorption of ions in an electrolyte.

One possible explanation for the observed behavior is that the binding sites of $ClO_4^-$ ions on Au(111) are occupied, or access to them is physically blocked by surface-bound PAPA during the self-assembly process whereas PAPT increases the availability of active adsorption sites. The PAPT SAMs show a different behavior by enhancing the interaction between gold and perchlorate. It is possible that there is more space between neighboring PAPT units, which can be accessed by perchlorate. A further possibility is a difference in the atomic surface structure related to the adsorption mechanism; unfortunately, scanning tunneling investigations

11

of the SAMs did not show SAMs of sufficient long-range order to analyze details of packing. Simulations of the processes may be needed to analyze the differences [54].

Previously observed structural differences between thiol and thioacetate SAMs have been attributed to differences in the formation mechanism, for which a tentative model has been developed [21]. According to this model, dissociation of the thioacetate occurs at the surface, as evidenced by determined reaction orders [21]. It has been indirectly concluded that after dissociation, both thiolate and acetyl group are surface-bound; the removal of the latter would open an adsorption site for a next thiolate [21]. The molecular rearrangements during adsorption must in one form or another block perchlorate adsorption sites; possible is a direct electronic interaction between the "flat lying" (Fig. 8) azobenzene moiety and gold, or an interaction via the N-atoms. What enhances perchlorate adsorption in SAMs formed from the thiol is unclear in this picture, however.

In a recent work on SAMs on copper, our group found evidence for a C-S cleavage in ethanol, which was absent in the solvent tetrahydrofuran [55], and other studies also noted strong reactions on copper surfaces in the presence of thiolates [56]. This observation shows that also differences in the solvent at formation stage may lead to different surface structures. If the solvent was modified during the base-catalysed deposition by the thioacetate, a "solvent modification effect" is a further possibility to explain the results from this work. If the deposition process led to the cleavage not only of the $-S-(C=O)$ bond, but only in a small fraction of the molecules also to cleavage of the bond between sulfur and the methylene group, the forming sulfide might be able to block sites needed for perchlorate adsorption on the surface. No evidence exists for a contribution of charge transfer through the SAMs to the differences, as reported elsewhere [57].

While in this work, no photoisomerization experiments have been conducted, recent results on surface dilution make effects of small structural differences on isomerization highly likely [58].

# 4    Summary and conclusions

IR spectra show that SAMs formed from PAPT and PAPA in ethanol solution contain the same molecules. SAM formation from both precursors yields similar surface coverages. However, PAPT SAMs enhance the interaction between Au(111) and the perchlorate ion in aqueous solution, even when comparing to pure Au(111), whereas PAPA SAMs suppress perchlorate adsorption. Possible reasons for this counterintuitive observations are (i) different atomic surface structures on the Au/SAM interface after SAM formation, (ii) physical hindrance of perchlorate access to the surface after the SAM formation process from the different precursors, and

(iii) the presence of a sulfidic impurity on the surface. Electrochemical accessible surface of SAM covered metals is hence affected by the adsorption geometry, which is affected by the precursor used in SAM preparation. This observation is of relevance for SAMs used, e.g., in sensing or for chemically active surfaces, where interaction with species from the surrounding with the surface is crucial. Beyond the obvious modification of the chemical termination of the surface, the electrochemical properties of the resulting surfaces depend critically on the adsorption mechanism, which can be affected with the chosen precursor. Different surface properties can thus be realised in "nominally identical" surfaces, opening up for intricate experimental leverage to surface modification, e.g. for ion specific electrochemical detection.

# 5    Acknowledgments

# References

[1] Love, J. C.; Estroff, L. A.; Kriebel, J. K.; Nuzzo, R. G.; Whitesides, G. M. Self-assembled monolayers of thiolates on metals as a form of nanotechnology. *Chem. Rev.* **2005**, *105*, 1103–69.

[2] Madueno, R.; Räisänen, M. T.; Silien, C.; Buck, M. Functionalizing hydrogen-bonded surface networks with self-assembled monolayers. *Nature* **2008**, *454*, 618–21.

[3] Ariga, K.; Mori, T.; Akamatsu, M.; Hill, J. P. Two-dimensional nanofabrication and supramolecular functionality controlled by mechanical stimuli. *Thin Solid Films* **2014**, *554*, 32–40.

[4] Cho, H.; Zook, J.; Banner, T.; Park, S.-H.; Min, B.-H.; Hasty, K. A.; Pinkhassik, E.; Lindner, E. Immobilization of fibrinogen antibody on self-assembled gold monolayers for immunosensor applications. *Tissue Eng. Regener. Med.* **2014**, *11*, 10–15.

[5] Erbe, A.; Bushby, R. J.; Evans, S. D.; Jeuken, L. Tethered bilayer lipid membranes studied by simultaneous attenuated total reflectance infrared spectroscopy and electrochemical impedance spectroscopy. *J. Phys. Chem. B* **2007**, *111*, 3515.

[6] Pourbeyram, S.; Shervedani, R. K.; Sabzyan, H. Surface Science STM characterization of DNA immobilized via Zr ion glue onto gold thiol SAMs. *Surf. Sci.* **2013**, *616*, 100–103.

[7] Cheng, X.; Lowe, S. B.; Reece, P. J.; Gooding, J. J. Colloidal silicon quantum dots: from preparation to the modification of self-assembled monolayers (SAMs) for bio-applications. *Chem. Soc. Rev.* **2014**, *43*, 2680–700.

[8] Hasan, A. Self-assembled monolayers in biomaterials. *Nanobiomaterials* **2017**, 137–178.

[9] Singh, M.; Kaur, N.; Comini, E. The role of self-assembled monolayers in electronic devices. *J. Mater. Chem. C* **2020**, *8*, 3938–3955.

[10] Huang, X.; Li, T. Recent progress in the development of molecular-scale electronics based on photoswitchable molecules. *J. Mater. Chem. C* **2020**, *8*, 821–848.

[11] Hosseinpour, S.; Gothelid, M.; Leygraf, C.; Johnson, C. M. Self-Assembled Monolayers as Inhibitors for the Atmospheric Corrosion of Copper Induced by Formic Acid: A Comparison between Hexanethiol and Hexaneselenol. *J. Electrochem. Soc.* **2013**, *161*, C50–C56.

[12] Zhang, D. Q.; Zeng, H. j.; Zhang, L.; Liu, P.; Gao, L. X. Influence of oxygen and oxidant on corrosion inhibition of cysteine self-assembled membranes for copper. *Coll. Surf. A* **2014**, *445*, 105–110.

[13] Hsieh, S.; Chao, W.-J.; Lin, P.-Y.; Hsieh, C.-W. Influence of molecular packing on the corrosion inhibition properties of self-assembled octadecyltrichlorosilane monolayers on silicon. *Corros. Sci.* **2014**, *80*, 427–433.

[14] Rechmann, J.; Sarfraz, A.; Götzinger, A. C.; Dirksen, E.; Müller, T. J. J.; Erbe, A. Surface Functionalization of Oxide-Covered Zinc and Iron with Phosphonated Phenylethynyl Phenothiazine. *Langmuir* **2015**, *31*, 7306–7316.

[15] Clayden, J.; Greeves, N.; Warren, S.; Wothers, P. *Organic Chemistry*; Oxford University Press Inc.: New York, 2005.

[16] Badin, M. G.; Bashir, A.; Krakert, S.; Strunskus, T.; Terfort, A.; Wöll, C. Kinetically stable, flat-lying thiolate monolayers. *Angew. Chem. Int. Ed.* **2007**, *46*, 3762–3764.

[17] Singh, A.; Dahanayaka, D. H.; Biswas, A.; Bumm, L. A.; Halterman, R. L. Molecularly Ordered Decanethiolate Self-Assembled Monolayers on Au(111) from in Situ Cleaved Decanethioacetate: An NMR and STM Study of the Efficacy of Reagents for Thioacetate Cleavage. *Langmuir* **2010**, *26*, 13221–13226.

[18] Jin, J.; Zhou, W.-J.; Chen, Y.; Liu, Y.-L.; Sun, X.-Q.; Xi, H.-T. The Thioacetate-Functionalized Self-Assembled Monolayers on Au: Toward High-Performance Ion-Selective Electrode for Ag$^+$. *Bull. Korean Chem. Soc.* **2014**, *35*, 601–604.

[19] Schreiber, F. Structure and growth of self-assembling monolayers. *Prog. Surf. Sci.* **2000**, *65*, 151–257.

[20] Tour, J. M.; Jones, L.; Pearson, D. L.; Lamba, J. J. S.; Burgin, T. P.; Whitesides, G. M.; Allara, D. L.; Parikh, A. N.; Atre, S. Self-Assembled Monolayers and Multilayers of Conjugated Thiols, $\alpha,\omega$-Dithiols, and Thioacetyl-Containing Adsorbates. Understanding Attachments between Potential Molecular Wires and Gold Surfaces. *J. Am. Chem. Soc.* **1995**, *117*, 9529–9534.

[21] Bashir, A.; Iqbal, D.; Jain, S. M.; Barbe, K.; Abu-Husein, T.; Rohwerder, M.; Terfort, A.; Zharnikov, M. Promoting Effect of Protecting Group on the Structure and Morphology of Self-Assembled Monolayers: Terphenylylethanethioactate on Au(111). *J. Phys. Chem. C* **2015**, *119*, 25352–25363.

[22] Park, T.; Kang, H.; Ito, E.; Noh, J. Self-Assembled Monolayers of Alkanethioacetates on Au(111) in Ammonium Hydroxide Solution. *Bull. Korean Chem. Soc.* **2021**, *42*, 252–257.

[23] Yager, K. G.; Barrett, C. J. Novel photo-switching using azobenzene functional materials. *J. Photochem. Photobiol. A* **2006**, *182*, 250–261.

[24] Barrett, C. J.; Mamiya, J.-i.; Yager, K. G.; Ikeda, T. Photo-mechanical effects in azobenzene-containing soft materials. *Soft Matter* **2007**, *3*, 1249.

[25] Stock, P.; Erbe, A.; Buck, M.; Wiedemann, D.; Ménard, H.; Hörner, G.; Grohmann, A. Thiocyanate Anchors for Salt-like Iron(II) Complexes on Au(111): Promises and Caveats. *Z. Naturforsch. B* **2014**, *69*, 1164 – 1180.

[26] Evans, S. D.; Johnson, S. R.; Ringsdorf, H.; Williams, L. M.; Wolf, H. Photoswitching of Azobenzene Derivatives Formed on Planar and Colloidal Gold Surfaces. *Langmuir* **1998**, *14*, 6436–6440.

[27] Yu, S. H.; Hassan, S. Z.; Nam, G.-H.; An, S.; Kang, B.; Chung, D. S. Consideration of Azobenzene-Based Self-Assembled Monolayer Deposition Conditions for Maximizing Optoelectronic Switching Performances. *Chem. Mater.* **2021**, *33*, 5991–6002.

[28] Bronsch, W.; Moldt, T.; Boie, L.; Gahl, C.; Weinelt, M. Delocalized versus localized excitations in the photoisomerization of azobenzene-functionalized alkanethiolate SAMs. *J. Phys.: Condens. Matter* **2017**, *29*, 484002.

[29] McElhinny, K. M.; Park, J.; Ahn, Y.; Huang, P.; Joo, Y.; Lakkham, A.; Pateras, A.; Wen, H.; Gopalan, P.; Evans, P. G. Photoisomerization Dynamics in a Densely Packed Optically Transformable Azobenzene Monolayer. *Langmuir* **2018**, *34*, 10828–10836.

[30] Krekiehn, N. R.; Müller, M.; Jung, U.; Ulrich, S.; Herges, R.; Magnussen, O. M. UV/Vis Spectroscopy Studies of the Photoisomerization Kinetics in Self-Assembled Azobenzene-Containing Adlayers. *Langmuir* **2015**, *31*, 8362–8370.

[31] Moldt, T.; Brete, D.; Przyrembel, D.; Das, S.; Goldman, J. R.; Kundu, P. K.; Gahl, C.; Klajn, R.; Weinelt, M. Tailoring the Properties of Surface-Immobilized Azobenzenes by Monolayer Dilution and Surface Curvature. *Langmuir* **2015**, *31*, 1048–1057.

[32] Zhou, W.; Grosjean, S.; Bräse, S.; Heinke, L. Thermal cis-to-trans Isomerization of Azobenzene Side Groups in Metal-Organic Frameworks investigated by Localized Surface Plasmon Resonance Spectroscopy. *Z. Phys. Chem.* **2019**, *233*, 15–22.

[33] Schulze, M.; Utecht, M.; Moldt, T.; Przyrembel, D.; Gahl, C.; Weinelt, M.; Saalfrank, P.; Tegeder, P. Nonlinear optical response of photochromic azobenzene-functionalized self-assembled monolayers. *Phys. Chem. Chem. Phys.* **2015**, *17*, 18079–18086.

[34] Riaz, S.; Friedrichs, G. Vibrational sum-frequency generation study of molecular structure, sterical constraints and nonlinear optical switching contrast of mixed alkyl-azobenzene self-assembled monolayers. *Z. Phys. Chem.* **2020**, *234*, 1427–1452.

[35] Marten, J.; Erbe, A.; Critchley, K.; Bramble, J. P.; Weber, E.; Evans, S. D. Self-Assembled Layers Based on Isomerizable Stilbene and Diketoarylhydrazone Moieties. *Langmuir* **2008**, *24*, 2479–2486.

[36] Qi, Y.; Liu, X.; Hendriksen, B. L. M.; Navarro, V.; Park, J. Y.; Ratera, I.; Klopp, J. M.; Edder, C.; Himpsel, F. J.; Fréchet, J. M. J.; Haller, E. E.; Salmeron, M. Influence of Molecular Ordering on Electrical and Friction Properties of $\omega$-(trans-4-Stilbene)Alkylthiol Self-Assembled Monolayers on Au (111). *Langmuir* **2010**, *26*, 16522–16528.

[37] Liao, L.-y.; Li, Y.-b.; Zhang, X.-m.; Geng, Y.-f.; Zhang, J.-y.; Xie, J.-l.; Zeng, Q.-d.; Wang, C. STM Investigation of the Photoisomerization and Photodimerization of Stilbene Derivatives on HOPG Surface. *J. Phys. Chem. C* **2014**, *118*, 15963–15969.

[38] Zheng, L.-Q.; Yang, S.; Lan, J.; Gyr, L.; Goubert, G.; Qian, H.; Aprahamian, I.; Zenobi, R. Solution Phase and Surface Photoisomerization of a Hydrazone Switch with a Long Thermal Half-Life. *J. Am. Chem. Soc.* **2019**, *141*, 17637–17645.

16

[39] Caldwell, W. B.; Campbell, D. J.; Chen, K.; Herr, B. R.; Mirkin, C. A.; Malik, A.; Durbin, M. K.; Dutta, P.; Huang, K. G. A Highly Ordered Self-Assembled Monolayer Film of an Azobenzenealkanethiol on Au(111): Electrochemical Properties and Structural Characterization by Synchrotron in-Plane X-ray Diffraction, Atomic Force Microscopy, and Surface-Enhanced Raman Spectroscopy. *J. Am. Chem. Soc.* **1995**, *117*, 6071–6082.

[40] Alkire, R.; Kolb, D.; Lipkowski, J.; Ross, P. *Chemically Modified Electrodes*; Wiley-VCH: Weinheim, Germany, 2009.

[41] Muglali, M. I.; Erbe, A.; Chen, Y.; Barth, C.; Koelsch, P.; Rohwerder, M. Modulation of electrochemical hydrogen evolution rate by araliphatic thiol monolayers on gold. *Electrochim. Acta* **2013**, *90*, 17 – 26.

[42] Koelsch, P.; Muglali, M. I.; Rohwerder, M.; Erbe, A. Third-order effects in resonant sum-frequency-generation signals at electrified metal/liquid interfaces. *J. Opt. Soc. Am. B* **2013**, *30*, 219–223.

[43] Kemnade, N.; Chen, Y.; Muglali, M. I.; Erbe, A. Electrochemical reductive desorption of alkyl self-assembled monolayers studied in situ by spectroscopic ellipsometry: evidence for formation of a low refractive index region after desorption. *Phys. Chem. Chem. Phys.* **2014**, *16*, 17081–17090.

[44] Su, Z.; Leitch, J.; Lipkowski, J. Measurements of the Potentials of Zero Free Charge and Zero Total Charge for 1-thio-$\beta$-D-glucose and DPTL Modified Au(111) Surface in Different Electrolyte Solutions. *Z. Phys. Chem.* **2012**, *226*, 995–1009.

[45] Wolf, H.; Ringsdorf, H.; Delamarche, E.; Takami, T.; Kang, H.; Michel, B.; Gerber, C.; Jaschke, M.; Butt, H.-J.; Bamberg, E. End-Group-Dominated Molecular Order in Self-Assembled Monolayers. *J. Phys. Chem.* **1995**, *99*, 7102–7107.

[46] Erbe, A.; Sarfraz, A.; Toparli, C.; Schwenzfeier, K.; Niu, F. In *Soft Matter at Aqueous Interfaces*; Lang, P. R., Liu, Y., Eds.; Lect. Notes Phys.; Springer: Cham, Switzerland, 2016; Vol. 917; pp 459–490.

[47] Hamoudi, H.; Prato, M.; Dablemont, C.; Cavalleri, O.; Canepa, M.; Esaulov, V. A. Self-assembly of 1,4-benzenedimethanethiol self-assembled monolayers on gold. *Langmuir* **2010**, *26*, 7242–7.

[48] Ito, E.; Kang, H.; Lee, D.; Park, J. B.; Hara, M.; Noh, J. Spontaneous desorption and phase transitions of self-assembled alkanethiol and alicyclic thiol monolayers chemisorbed on Au(111) in ultrahigh vacuum at room temperature. *J. Colloid Interface Sci.* **2013**, *394*, 522–9.

[49] Ahlrichs, R.; Bär, M.; Häser, M.; Horn, H.; Kölmel, C. Electronic structure calculations on workstation computers: The program system turbomole. *Chem. Phys. Lett.* **1989**, *162*, 165–169.

[50] Sinha, P.; Boesch, S. E.; Gu, C.; Wheeler, R. A.; Wilson, A. K. Harmonic Vibrational Frequencies: Scaling Factors for HF, B3LYP, and MP2 Methods in Combination with Correlation Consistent Basis Sets. *J. Phys. Chem. A* **2004**, *108*, 9213–9217.

[51] Zhumaev, U.; Lai, A.; Pobelov, I.; Kuzume, A.; Rudnev, A.; Wandlowski, T. Quantifying perchlorate adsorption on Au(111) electrodes. *Electrochim. Acta* **2014**, *146*, 112–118.

[52] Zhumaev, U.; Pobelov, I.; Rudnev, A.; Kuzume, A.; Wandlowski, T. Decoupling surface reconstruction and perchlorate adsorption on Au(111). *Electrochem. Commun.* **2014**, *44*, 31–33.

[53] Schuster, S.; Füser, M.; Asyuda, A.; Cyganik, P.; Terfort, A.; Zharnikov, M. Photoisomerization of azobenzene-substituted alkanethiolates on Au(111) substrates in the context of work function variation: the effect of structure and packing density. *Phys. Chem. Chem. Phys.* **2019**, *21*, 9098–9105.

[54] Wen, J.; Li, W.; Chen, S.; Ma, J. Simulations of molecular self-assembled monolayers on surfaces: packing structures, formation processes and functions tuned by intermolecular and interfacial interactions. *Phys. Chem. Chem. Phys.* **2016**, *18*, 22757–22771.

[55] Rechmann, J.; Krzywiecki, M.; Erbe, A. Carbon–Sulfur Bond Cleavage During Adsorption of Octadecane Thiol to Copper in Ethanol. *Langmuir* **2019**, *35*, 6888–6897.

[56] Whitley, M.; Newton, M.; McHale, G.; Shirtcliffe, N. J. The Self Assembly of Superhydrophobic Copper Thiolate Films on Copper in Thiol Solutions. *Z. Phys. Chem.* **2012**, *226*, 187–200.

[57] Tonnelé, C.; Pershin, A.; Gali, S. M.; Lherbier, A.; Charlier, J.-C.; Castet, F.; Muccioli, L.; Beljonne, D. Atomistic simulations of charge transport in photoswitchable organic-graphene hybrids. *J. Phys.: Mater.* **2019**, *2*, 035001.

[58] Rietze, C.; Titov, E.; Granucci, G.; Saalfrank, P. Surface Hopping Dynamics for Azobenzene Photoisomerization: Effects of Packing Density on Surfaces, Fluorination, and Excitation Wavelength. *J. Phys. Chem. C* **2020**, *124*, 26287–26295.

18
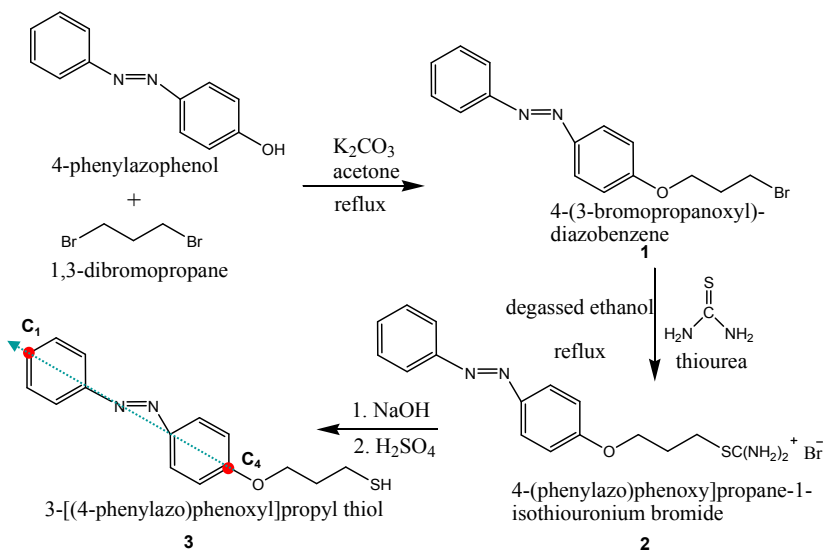
Figure 1: Synthesis process of PAPT. In **2**, the axis defined by the $C_1$ and $C_4$ atoms is indicated which will later be used to determine tilt with respect to the Au(111) surface normal.
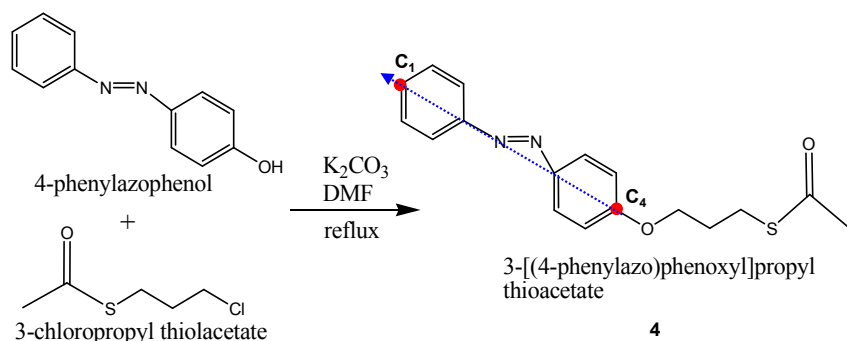


Figure 2: Synthesis of PAPA. In molecule **4**, the axis defined by the $C_1$ and $C_4$ atoms is indicated which will later be used to determine tilt angle $\delta$ with respect to the Au(111) surface normal; this is the same axis as indicated in Fig. 1.
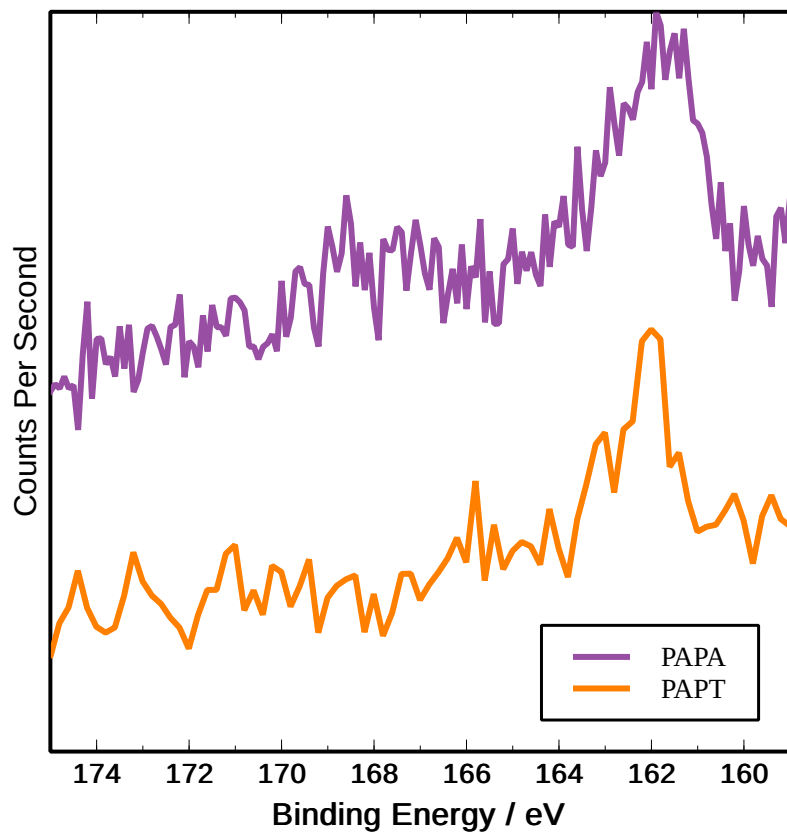
Figure 3: S 2p XP spectra of PAPT and PAPA adsorbed to Au(111).
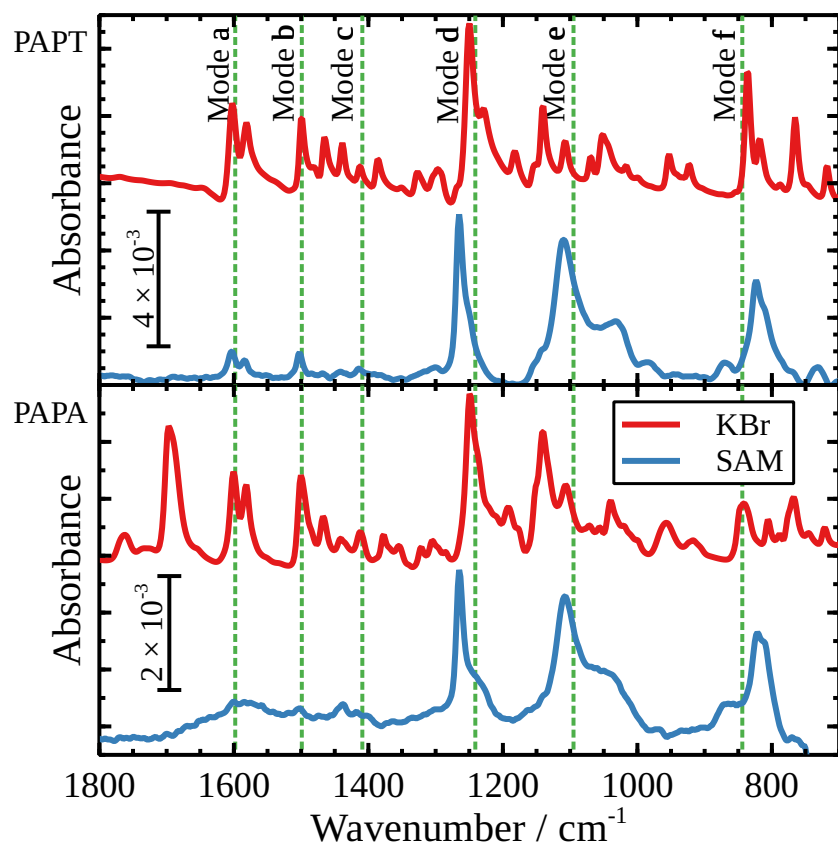
Figure 4: IR spectra of PAPT (top) and PAPA (bottom) in KBr pellets and as SAMs on gold. The absorbance of bulk spectra was normalized such that peak d has approximately same absorbance in SAM and in KBr spectra for ease of representation. Bulk spectra have been vertically offset. The wavenumbers obtained by simulations of characteristic modes (Tab. 1) are highlighted by vertical lines.
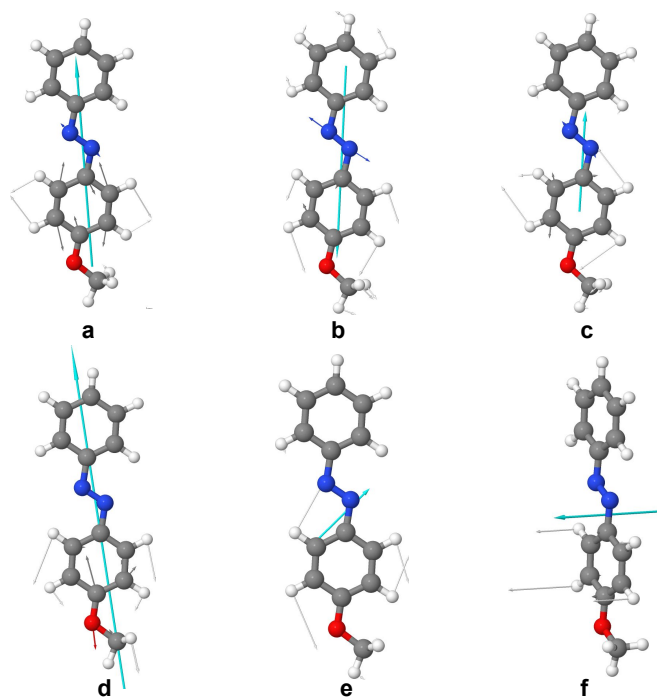
Figure 5: Simulated vibrational modes of the azobenzene core of PAPA and PAPT. Arrows in the color of the the atoms indicate relative magnitude and direction of the atom movements during the modes with the respective label as indicated in Tab. 1. Cyan arrows indicate the direction of the TDM of the respective mode.
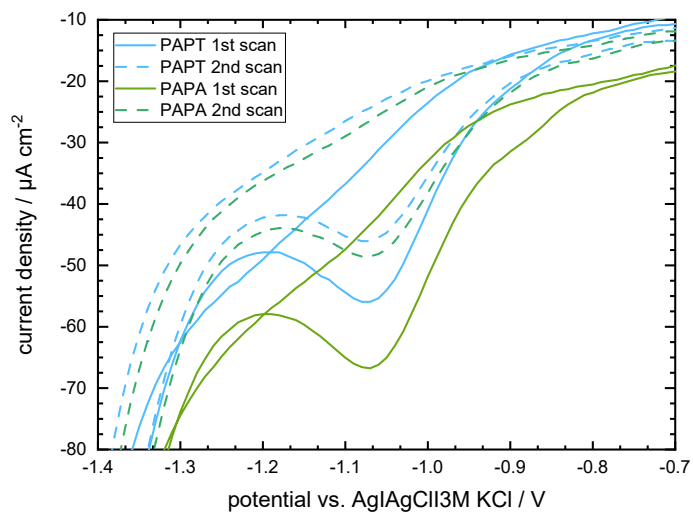
Figure 6: CVs of PAPT and PAPA SAMs during reductive desorption. Electrolyte: 0.1 M aqueous NaClO$_4$, scan rate: 50 mV/s, scan range: -1.5 V to -0.6 V. Charges obtained from peak integration of the desorption peak from the first scan are compiled in Tab. 2.
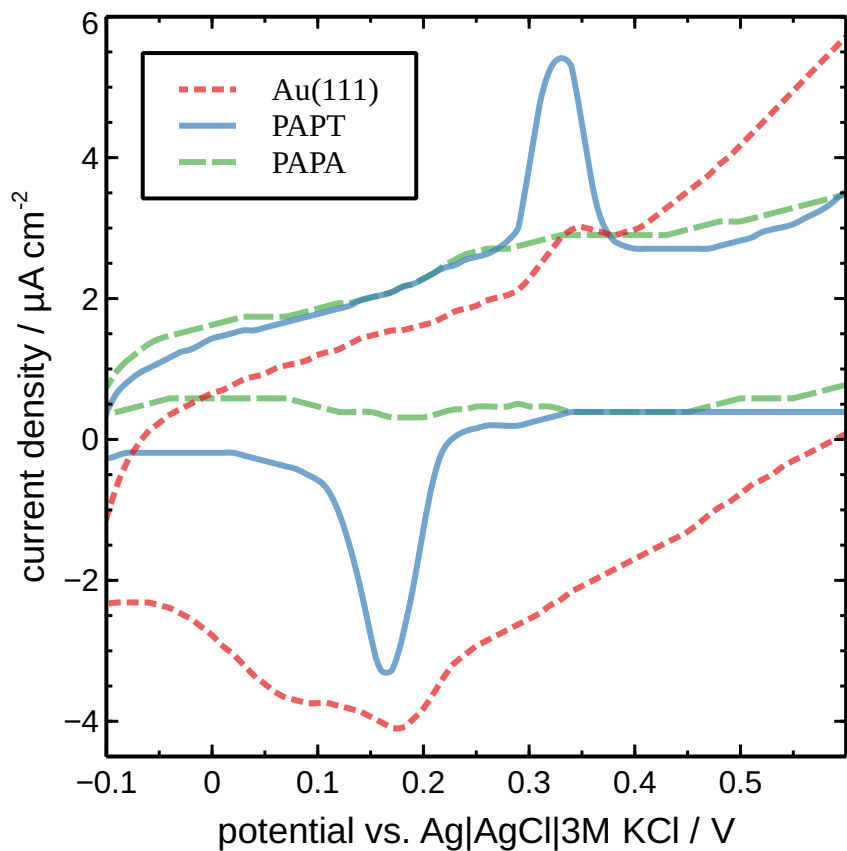
Figure 7: CVs of PAPA and PAPT SAMs, and for comparison the bare Au(111) surface in 0.1 M aqueous NaClO$_4$ electrolyte. Scan rate: 50 mV/s, scan range: -0.1 V to 0.9 V. Charges obtained from peak integration are compiled in Tab. 2

24
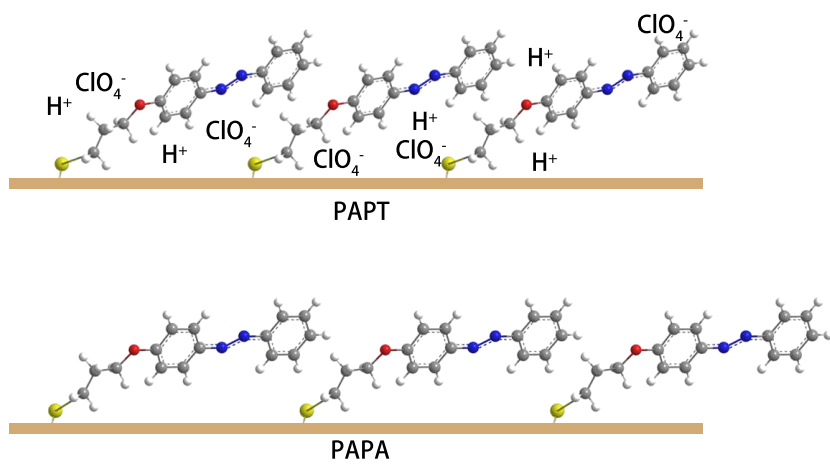
Figure 8: A schematic representation of PAPT and PAPA SAMs in electrolyte with the adsorption of $ClO_4^-$ ions.

Table 1: Assignments of characteristic IR absorption based on DFT calculations. The mode label in the first column refers to Fig. 5. The orientation is indicated approximately with respect to the $C_1$-$C_4$ axis axis indicated in Fig. 1 and 2

| Label | Orient. | DFT | Assignment | PAPT | | PAPA | |
|-------|---------|-----|------------|------|-----|------|-----|
| | | | | KBr | SAM | KBr | SAM |
| | | $cm^{-1}$ | | $cm^{-1}$ | $cm^{-1}$ | $cm^{-1}$ | $cm^{-1}$ |
| a | ‖ | 1598 | $\nu(C_{ar}$-$C_{ar})$ | 1603 | 1603 | 1601 | 1601 |
| b | ‖ | 1499 | $\nu(C_{ar}$ - N=N - $C_{ar})$ | 1499 | 1502 | 1500 | 1502 |
| c | ‖ | 1409 | $\nu(C_{ar}$-$C_{ar})$ | 1412 | 1414 | ? | ? |
| d | ‖ | 1241 | $\nu_{as}(C$-O-$C_{ar})$ | 1250 | 1265 | 1248 | 1265 |
| e | ⊥ | 1095 | $\delta$ (H, in-plane) | 1107 | 1109 | 1107 | 1107 |
| f | ⊥ | 844 | $\delta$ (H, oop) | 818 | 823 | ? | ? |

?: Mode could not be unambiguously assigned, several peaks

Table 2: Absolute values of charges, in µC cm$^{-2}$, obtained from integrating the CV peaks. Standard deviation over 6 measurements given in brackets for the reductive desorption experiments. No systematic uncertainty analysis was conducted for the perchlorate ad- and desorption

| | SAM reductive desorption | $ClO_4^-$ adsorption | $ClO_4^-$ desorption |
|-------|--------------------------|----------------------|----------------------|
| bare Au(111) | - | 2.6 | 2.2 |
| PAPT | 30(14) | 5.0 | 7.4 |
| PAPA | 37(11) | - | - |

Table 3: Thickness obtained from ellipsometry, $t^{(ell)}$, and IR [$t^{(IR)}$, via eq. (2)]. Tilt angle $\delta(C_1$-$C_4)$ of $C_1$-$C_4$ axis [via eq. (1) with modes a, b, c for ‖ and modes e, f for ⊥]. Tilt angle $\delta(C_4$-O-C) of $C_4$-O-C TDM [via eq. (1) with mode d for ‖ and modes e, f for ⊥], modes c and f were quantified only for PAPT. The given range is the span obtained from the analysis of the combination of different modes; for PAPA, $\delta(C_4$-O-C) could only be quantified from one mode combination. Tilt angle $\delta^{(ell)}$ obtained from $t^{(ell)}$ via inverting eq. (2). Surface coverage $\Gamma$ calculated from CV results (integrated current of reductive desorption, Tab. 2)

| SAMs | $t^{(ell)}$ | $t^{(IR)}$ | $\delta(C_1$-$C_4)$ | $\delta(C_4$-O-C) | $\delta^{(ell)}$ | $\Gamma_{CV}$ |
|------|-------------|------------|---------------------|-------------------|------------------|---------------|
| | nm | nm | ° | ° | ° | pmol cm$^{-2}$ |
| PAPT | $(0.74 \pm 0.06)$ | 0.39-0.51 | 70-75 | 60-65 | 59-64 | $315 \pm 120$ |
| PAPA | $(0.37 \pm 0.04)$ | 0.36-0.44 | 73-76 | ca. 62 | 75-78 | $387 \pm 105$ |